Applied Physics A (2019) 125:747
https://doi.org/10.1007/s00339-019-3043-5

Applied Physics A
Materials Science & Processing

Epitaxial characteristics of MBE-grown ZnTe thin films on GaAs (211)B substrates

Elif Ozceri[1,2] · Enver Tarhan[2]

Received: 18 July 2019 / Accepted: 26 September 2019 / Published online: 9 October 2019
© Springer-Verlag GmbH Germany, part of Springer Nature 2019

Abstract
Highly crystalline ZnTe thin films were grown on GaAs (211)B substrates by molecular beam epitaxy (MBE) for potential applications such as MCT detectors and optoelectronic devices. We investigated the effects of Te to Zn (VI/II) flux ratio on the quality of ZnTe films in terms of crystal orientation, elemental composition, surface roughness, and dislocation density. Atomic concentrations of Zn, Te, and oxygen complexes due to oxygen contamination on the film surfaces were analyzed by X-ray photoelectron spectroscopy. X-ray double crystal rocking curve full width half maximum (FWHM) of ZnTe (422) peak was observed as 233 arcseconds for a 1.66 µm thick film, which indicates high crystallinity. Wet chemical etching was applied to the films to quantify the crystal quality by calculating etch pit densities (EPD) from scanning electron microscope images. A very low EPD value of 1.7×10^7 cm^{-2} was measured. Additionally, the root mean square roughness values, obtained from atomic force microscopy topography images were in the range of 10–25 nm. These values were supported by FWHM values of red green blue color intensity histograms obtained from Nomarski Microscope images. The results of our analyses indicate that the VI/II flux ratios of 4 and 4.5 produce the best quality ZnTe films on GaAs (211)B substrates.

1 Introduction

ZnTe is a II–VI semiconductor with a zinc-blende crystal structure. It has a lattice constant of 6.1037 Å [1]. Having a 2.27 eV room temperature (RT) direct band gap energy gives rise to a strong absorption band in the short wavelength range of the infrared (IR) spectrum. ZnTe has a strong potential for many optoelectronic device applications such as light emitting diodes, terahertz detectors, solar cells, waveguides, and modulators [2–8]. In particular, there are reports on heterojunction diode applications of intrinsically *p*-type ZnTe [9, 10]. On the other hand, the properties of ZnTe can be tailored by oxygen addition to form the $ZnTe_{1-x}O_x$ (ZnTeO) ternary structure where x is the oxygen fraction ($0 \leq x \leq 1$). Addition of a small fraction of oxygen (x being close to zero) into ZnTe, gives rise to new absorptive energy bands in the band gap of ZnTe, hence, extending its absorption spectrum well into long wavelength ranges in the IR region covering the entire solar spectrum. This makes it one of the most efficient materials in solar cell applications [11].

ZnTe is also used as a buffer layer mostly for HgCdTe (MCT)-based infrared detectors. Although CdZnTe (CZT) is an ideal substrate due to its perfect lattice match and thermal expansion coefficient match with MCT, it has several drawbacks such as limited availability in large areas, high cost, low crystal quality, and high fragility [12, 13]. Hence, alternative substrates such as Si, Ge, and GaAs are commonly used in spite of their lattice and thermal expansion coefficient mismatches with MCT [14, 15]. Crystal quality and purity of MCT plays an important role on its device performance. Lattice and thermal expansion coefficient mismatches cause structural defects at the MCT-substrate interface. Especially, threading dislocations, extending from the substrate-epilayer interface well into the MCT film, greatly deteriorate the device performance. Hence, such defects should be suppressed by addition of a buffer layer between the substrate and the MCT film [14]. Among the alternative substrate materials to CZT, GaAs is better than Si due to its lower lattice (14%) [14], and thermal expansion coefficient (13.8%) mismatches. Its low-cost, easy accessibility, and crystal structure (both MCT and GaAs are zinc blende) also make GaAs a very good alternative substrate to CZT [16]. Other type of structural defects deteriorating the device

✉ Elif Ozceri
elifozceri@iyte.edu.tr

[1] Department of Materials Science and Engineering, Izmir Institute of Technology, Urla, 35430 Izmir, Turkey

[2] Department of Physics, Izmir Institute of Technology, Urla, 35430 Izmir, Turkey

performance are native point defects and dislocations mainly due to oxide removal and chemical cleaning processes. To suppress such defects and to prevent orientation shifts in MCT, ZnTe is commonly used as a nucleation or buffer layer [17–19]. GaAs substrate with a ZnTe buffer has a very low lattice mismatch of 7.8% [1], which provides a smooth transition by suppressing the dislocations in a few contact layer, thus, a relatively low dislocation densities towards the top layer is achieved.

To obtain high quality films with low dislocation densities, ZnTe epilayers can be grown on nearly lattice-matched II–VI GaSb and InAs substrates in a molecular beam epitaxy (MBE) system [20, 21]. However, as a III–V material, GaAs with a greater lattice mismatch with ZnTe is a preferable substrate material due to its high quality, large wafer area, commercially availability, and low cost in comparison to GaSb [1, 22]. Thus, high quality epitaxial growth of ZnTe on GaAs has recently received an increasing attention [23]. Arsenic rich (B) surface of GaAs (211) substrate is usually used for the growth of ZnTe buffer layer since it can bound especially Te atoms of ZnTe at the interface resulting in an epitaxial growth of ZnTe on GaAs.

In this work, we investigated the effect of Te to Zn (VI/II) growth flux ratio on the characteristics of ZnTe films grown on commercially purchased epi-ready GaAs (211) B substrates in an MBE chamber. The quality of heteroepitaxial layers, hence the device performance, depends on the crystal quality of ZnTe films which is mainly affected by growth conditions. We propose an effective method to obtain highly crystalline ZnTe (211) epitaxial films on GaAs (211)B substrates. The results of our studies on the epitaxial characteristics of ZnTe thin films were investigated by employing X-ray diffraction (XRD) spectroscopy, atomic force microscopy (AFM), Nomarski microscopy (NM), and X-ray photoelectron spectroscopy (XPS). Additionally, etch pith density (EPD) calculations were carried out using the scanning electron microscopy (SEM) images of etched samples. In particular, we demonstrated a useful way to determine the roughness value of a ZnTe film from a Nomarski microscope image.

2 Experimental/methods

Experimental procedures were carried out in the following order:

2.1 ZnTe film growth on epiready GaAs (211)B substrate

Thermal deoxidation of the 20×20 mm^2 epi-ready GaAs substrates followed by ZnTe growth on them were done in the growth chamber of a Veeco GEN20MZ MBE system under the background pressure of $3–5 \times 10^{-10}$ Torr. The deoxidation of the protective oxide layer of an epi-ready GaAs (211)B substrate was performed under In flux according to a procedure given in a previous study [24]. Firstly, the substrate was heated to about 530 °C (measured by a band edge thermometry; BandiT). Then, In flux was supplied at 4.5×10^{-8} Torr beam equivalent pressure (BEP) for 3 min until the substrate temperature reached to ~555 °C, which was maintained for 3 more minutes for the desorption of In compounds (InAs, InO_2). During the thermal deoxidation (complete removal of the oxide layer), structural properties of the surface was monitored in situ from the diffraction pattern by an incorporated reflection high-energy electron diffraction (RHEED) system. Next, the GaAs substrate was cooled under As_4 flux at 2.5×10^{-6} Torr BEP to preserve the As terminated face of the polar substrate. As_4 flux was closed at ~420 °C and Te_2 flux was opened when the substrate temperature fell to ~380 °C. Finally, when the substrate temperature was reduced to ~290 °C it was kept constant and ZnTe growth was initiated under Te_2 and Zn flux. All the growths were carried at a rate of about 1 μm/h for 120 min with varying VI/II flux ratios, which is the ratio of Te (group VI) and Zn (group II) BEP's. During the growth processes, substrates were rotated with two revolutions per minute (rpm) to ensure a uniform growth profile.

2.2 Compositional characterization by XPS

The elemental compositions of the as grown ZnTe films on the GaAs (211)B surface wafers were studied using an X-ray photoelectron spectrometer (XPS). Samples were immediately transferred from the growth chamber to the XPS system under atmospheric conditions, with a transfer duration not exceeding 5 min in order to minimize the contamination and oxidation of the film surfaces during their transfer. XPS measurements were carried out with a SPECS EA200 (Electron Spectroscopy for ChemicalAnalysis) system equipped with an Al X-ray source and a Phoibos 150 hemispherical analyzer with a 3D-DLD detector. A large area focus and a 40 eV E-pass energy were chosen to achieve the best signal to noise ratio in the XPS spectra. The spectra were calibrated with respect to C-1s signal position at 284 eV. After applying a Tougaard or linear background subtraction, the spectra were deconvoluted with a mixed (product of) Gaussian–Lorentzian peak profile using the CasaXPS software.

2.3 Crystal structure characterization by XRD

The crystal structure of our ZnTe films grown on GaAs (211) B substrates were analyzed with XRD θ–2θ scans taken in the 5°–90° 2θ range using a Philips X'Pert Pro MRD XRD system equipped with a Cu K-alpha X-ray source. The structural quality of the films were further investigated with X-ray

double crystal rocking curve (DCRC) analyses of the peaks from ZnTe(422) planes measured at [0–11] and [–111] azimuths. Tilt angles (an indication of the orientational mismatch between the substrate and the film) were calculated as the difference between the peak angle positions measured at both azimuth directions. Full width at half maximum (FWHM) values gave information about the crystal quality of films. Debye Scherer equation was used to find the crystalline grain sizes from the measured FWHM values for a given reflection angle.

2.4 SEM images and etch pit density calculations

Defect decoration by wet chemical etching is the main method to reveal and observe various kinds of defects especially due to dislocation related ones over the epilayer surface. Since both ZnTe and CdTe are II–VI polar semiconductors with a zinc blende crystal structure, the methods used to study the dislocation densities of CdTe films can also be applied to ZnTe films for the same purpose [25].

Wet chemical etching processes were carried out in three main steps; oxidation, dissolution, and dilution [26]. These steps determine the chemical reaction and etching rate of the etching solution. Bromic acid, bromine, chromic acid, nitric acid, and hydrogen peroxide were used as oxidizing agents. A molecule of an oxidizing agent takes electrons from the film atoms. Te has a higher reactivity as compared to Zn. Thus, the oxidizing agents are more reactive with Te atoms. In the dilution step; DI water, lactic acid, or acetic acid were used as diluting agents [26]. After a wet chemical etching process, etch pits occur on a film surface due to the weakened bond strengths. As a result, end points of dislocations appear as dents of various geometric shapes on the film surface which can be observed on a SEM micrograph image. Moreover, different etching solutions leave different etch pit shapes on the surface depending on the etching rate of the solution, surface polarity, and the crystal orientation. Therefore, the crystal symmetry along the direction perpendicular to the surface can be monitored by the shapes and sizes of the etch pits.

In this study, after carrying out XPS and XRD measurements, each 20 × 20 mm^2 ZnTe/GaAs film was cut into several pieces of various sizes and shapes, each for an independent etching procedure, to carry out defect decoration analyses. We used two etching techniques independently on different pieces from the same original sample. First etching procedure was done using an Everson solution ($1HF:4HNO_3:25C_2H_4OHCOOH$) [27] for 25 s at RT while the alternative etching procedure was employed with a Nakagawa solution ($1HF:2H_2O_2:2H_2O$) [28] for 7 s at RT. As soon as an etching was completed, the sample was rinsed in DI water and dried under high-purity N_2 flow. Then, the areal densities of etch pits were obtained from the SEM micrographs by manual counting the number of pits for several chosen areas and dividing each count by the chosen area. The etch pit density (EPD, in units of count per unit area) was obtained as the average of the count densities. The SEM system used was a FEI Quanta 250 FEG without any coating with 20 keV energy accelerated electrons and a 5 spot size.

2.5 Structural characterization by AFM and Nomarski microscopy

A Solver Pro 7 AFM instrument from NT-MDT was used to determine the RMS surface roughness values of as grown ZnTe films. The topography images were obtained by HA_NC silicon tips with a cantilever thickness of 1.75 µm and force constants of 3.5 and 12 N/m in the tapping mode in a class-100 clean room environment.

The film surface morphologies were also investigated by utilizing a Nomarski microscope (A13.1013 BF/DF DIC Metallurgical Microscope) with a 100 × objective. The observed images are 3D-like through a polarized light and a diffraction interference contrast prisms. The images were recorded from five different locations of the surface of an as grown ZnTe film. In this work, we show that surface roughness values can also be estimated from these images [29].

3 Results and discussions

The elemental compositions of ZnTe films were studied using XPS. For that purpose, as grown samples were immediately transferred to an XPS chamber after removing them from the MBE chamber.

After a survey scan, a series of high-resolution measurements focused on Zn, Te, O, and C peaks were carried out in order to obtain the elemental compositions. The spectra in Fig. 1a–c show oxygen (O-1s), zinc (Zn-2p), and tellurium (Te-3d) peaks, respectively, obtained from the sample ZT2. Other samples show similar XPS spectra. As seen from the figure, a mixture of Lorentzian–Gaussian peak profiles were nicely fit to the experimental data (black dots). A linear background subtraction was used for O-1s and Te-3d peaks while, a Tougaard (non-linear) background subtraction was carried out for the Zn-2p peaks. Since the energy of X-rays for Al-K_α irradiation is about 1.5 keV, it corresponds to a penetration depth of about 30 Å [30]. This means that most of the electrons removed from the sample material comes from a few tens of atomic layers beneath the surface. Hence, even if a few top layers of the surface is contaminated with oxygen and other elements they will show strong XPS peaks. Indeed in our data we see strong oxygen peaks indicating surface contamination which is probably limited to a few top layers [31]. In Table 1, we show the results of elemental

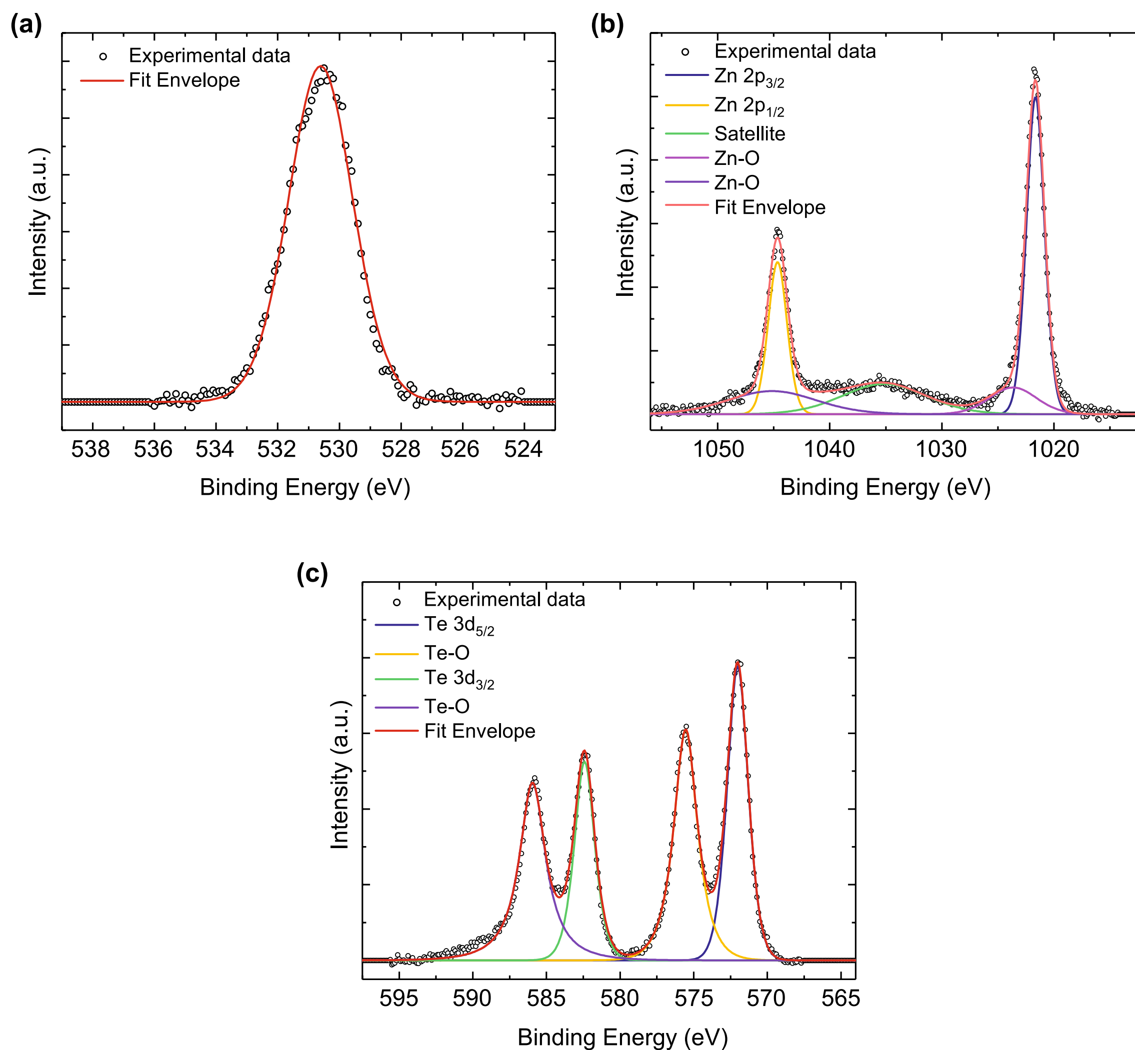

Fig. 1 XPS results of **a** O-1s, **b** Zn-2p, and **c** Te-3d scan from the as grown ZnTe surface of the sample ZT2. Black dots are experimental XPS data, the red line is the fitted envelope, and other lines are individual Lorentzian–Gaussian peaks

concentration (at.%) analyses obtained from XPS spectra of several samples. As seen from the table, oxygen concentration varies from sample to sample depending on both transfer conditions from MBE to XPS and on the surface morphologies of the films as well as the film quality. A single peak profile fits to the O-1s data, centered at 530.5 eV, as shown in Fig. 1a. Figure 1b shows the Zn 2p spectrum which is composed of a $2p_{3/2}$ peak centered at 1021.6 eV and a $2p_{1/2}$ peak centered at 1044.6 eV along with their Lorentz fits. The 23 eV difference (ΔE_{Zn}) between these two peaks is due to the spin orbit coupling effect observed mostly in the light and medium sized atoms and, to some degree, in the heavier atoms. The 2p peaks centered at 1023.65 eV and 1045.15 eV, corresponding to a spin–orbit splitting energy of 21.5 eV, are due to an oxidation state of Zn and they originate from Zn–O bonds [32]. The peak at 1035.15 is called a satellite peak [32].

The Te-3d spectrum is composed of a $3d_{5/2}$ peak at 572 eV and a $3d_{3/2}$ peak at 582 eV as seen in Fig. 1c. The peaks at 575.5 eV and 586 eV are related to TeO_2 complexes formed on the surfaces of ZnTe films [33]; [31] due to oxygen contamination from air. The strong TeO_2 peak intensities compared to those of Zn–O peaks indicate that the surface was terminated with Te atoms rather than Zn atoms. Table 2 gives the atomic concentration (at.%) ratios of Zn to Te as C_{Zn}/C_{Te} for all ZnTe film surfaces along with some other growth parameters as well as other important results obtained from our analyses given below.

Figure 2 shows typical XRD patterns of a ZnTe film on a (211) GaAs substrate (ZT7). Figure 2a gives the θ–2θ spectrum performed in the 5°–90° 2θ range. Note that we only see peaks associated with ZnTe (422) layers as well as those associated with GaAs (422) layers. For all ZnTe films grown on GaAs (211)B substrates we observed no other notable

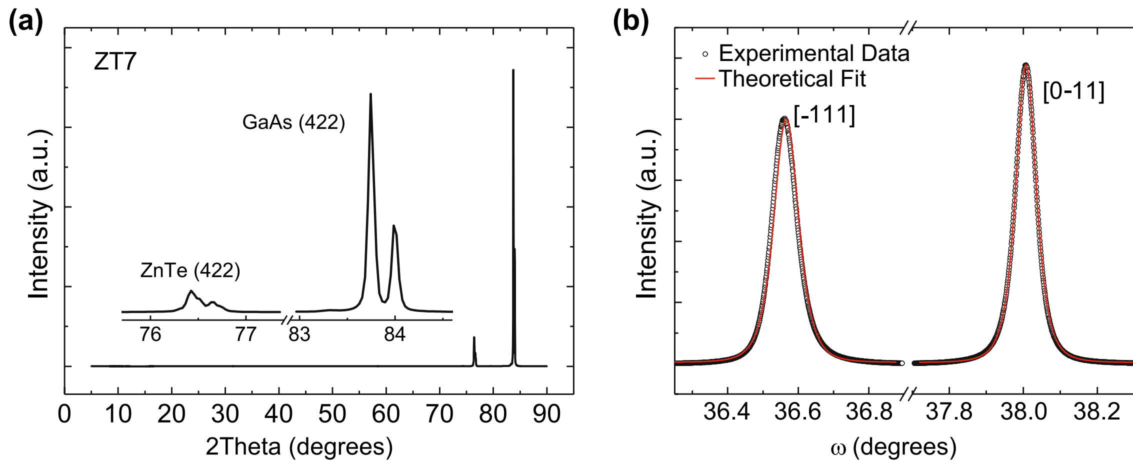

Fig. 2 XRD patterns of the sample ZT7 (ZnTe on (211) GaAs). **a** Full range θ–2θ scan, the inset highlights the observed peaks. **b** Double crystal rocking curve (DCRC) measurements of ZnTe(422) peaks taken at [0–11] and [–111] azimuth directions

Table 1 Elemental concentration analyses obtained from XPS spectra of Grown ZnTe films

Samples	Zn (at.%)	Zn–O (at.%)	Te (at.%)	Te–O (at.%)
ZT2	37.4	8.2	27.7	26.8
ZT3	34.0	12.0	27.4	26.6
ZT6	44.0	–	36.2	19.7
ZT7	40.7	–	39.2	20.2
ZT8	38.0	–	43.3	18.7
ZT9	42.5	–	36.7	20.8

peaks than those seen in Fig. 2a. Hence, we can claim with a confidence that all of our ZnTe films are highly crystalline with growth orientation similar to that of the GaAs substrate. The double peaks seen in Fig. 2a correspond to Kα1 (0.1540 nm) and Kα2 (0.1544 nm) lines of the Cu X-ray source. For further characterization of the crystal quality, high resolution X-ray double crystal rocking curve (DCRC) analyses of ZnTe (422) films on GaAs (211)B substrates were performed. Figure 2b shows the rocking curve spectra of the sample ZT7. The peaks centered at 36.561° and 38.007°, were measured at [–111] and [0–11] azimuth directions, respectively. The first peak has a full width half maximum (FWHM) value of 295.2 arcseconds while the FWHM for the second one is 234.4 arcsecs. Considering that the thicknesses of our ZnTe films were in the range of 1.2–1.7 µm (for comparison, such FWHM values are given only for thicker films in literature), both FWHM values indicate a good crystal structure for the (211) surface orientation [34]. We have also observed that all ZnTe films had narrower FWHM along [0–11] azimuth direction. The difference between the positions of the ZnTe (211) peaks for the two perpendicular measurement directions (namely, [–111] and [0–11]) is due to tilting of the ZnTe (211) planes with respect to those of GaAs (211)B substrates. This difference gives the tilt angle which is about 1.4° for the sample ZT7 as seen from Fig. 2. The tilt angles for all our samples varies from 1.4° to 1.9°

Table 2 Structural characterization results of XPS, X-ray DCRC, defect decoration, AFM and film thickness

Samples	C_{Zn}/C_{Te}	FWHM (422) [–111]	FWHM (422) [0–11]	Tilt angle (°)	τ (nm)	[c]EPD $\times 10^7$ cm^{-2}	R-AFM (nm)	t (µm)	VI/II flux ratio
ZT2	1.4	342.9	253.9	1.9	159.1	2.6[a]	13.9	1.24	3.0
ZT3	1.2	439.9	314.1	1.9	128.4	32[b]	22.0	1.19	1.7
ZT6	1.2	282.8	232.9	1.5	173.6	5.4[a]	18.0	1.51	4.0
ZT7	1.0	295.2	234.4	1.4	172.1	4.2[a]	13.8	1.66	4.0
ZT8	0.9	316.0	233.0	1.5	173.3	1.7[a]	12.3	1.66	4.5
ZT9	1.2	335.2	329.8	1.8	122.3	23[a]	16.4	1.57	5.0

The last column shows VI/II flux ratio of growth in MBE

[a]Nakagawa etched

[b]Everson etched

[c]Pit sizes were calculated with 0.05 nm accuracy

as reported in Table 2. The tilting is towards [–111] azimuth which allows a better lattice parameter match between the (422) planes of ZnTe film and GaAs (211)B substrate [35]. The tilt angles between the ZnTe and GaAs (211) substrates observed in our samples are less than the reported values in the literature for CdTe epilayers on GaAs (211) [36] and ZnTe films on Si (211) substrates [35]. For each sample we also calculated the average grain size, τ, of the crystallites along [0–11] direction from the Debye Scherer's formula:

$$\tau = \frac{K}{\beta \cos \theta},$$

where K is the dimensionless shape factor which is close to 0.9. The X-ray wavelength λ for a Cu K-alpha source is equal to 0.154 Å. β is the FWHM value in radians while θ is the Bragg angle. The calculated grain sizes are listed in Table 2. As seen from the table, the calculated grain sizes vary from 128.4 to 173.6 nm which indicates a good crystal quality with a near single crystal structure. This conclusion is also supported from the θ–2θ scan which only shows a single crystallographic orientation for the (211) planes being parallel to the film surface.

Figure 3a–c gives X-ray double crystal rocking curve (DCRC) FWHM values for (422) planes of all samples for growth VI/II flux ratio, film thickness, and Zn/Te concentration ratio (obtained from XPS), respectively. As seen from Fig. 3a FWHM has a minimum at 4.5 VI/II flux ratio for [0–11] measurement direction (ZT8) while it is at 4.0 for [–111] direction (ZT7 and ZT6), indicating that the crystal quality of the samples ZT6, ZT7, and ZT8 are better than the others. From Fig. 3b, the best FWHM values are for the film thicknesses between 1.5 and 1.65 micron again obtained from the samples ZT6, ZT7, and ZT8. When the flux ratio was increased to 5 (ZT9), FWHM increased while the thickness was reduced to 1.57 μm. Thus, we can infer that when the Te/Zn flux ratio increases beyond 4.5 the optimum

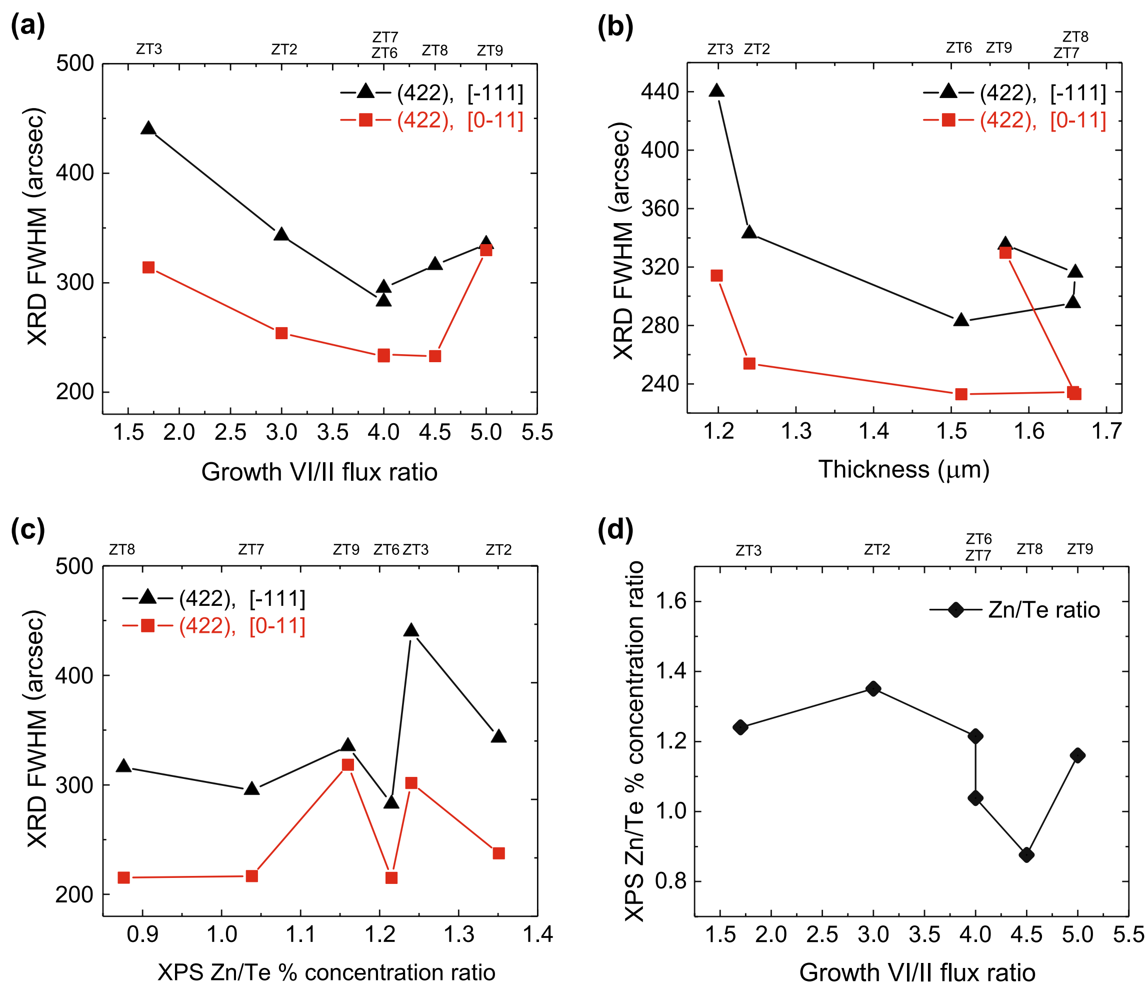

Fig. 3 **a** X-ray double crystal rocking curve FWHM versus VI/II flux ratio, **b** the X-ray DCRC FWHM versus ZnTe film thickness, **c** variation of X-ray DCRC FWHM with Zn/Te concentration ratio extracted from XPS analysis, and **d** Zn/Te concentration ratio with respect to VI/II flux ratio. The given XRD data were collected from ZnTe(422) planes along [–111] and [0–11] azimuth directions

growth conditions will be lost. According to Fig. 3c the films exhibiting the minimum DCRC FWHM values (hence, better crystallinity) have Zn/Te concentration ratios of about 0.9, 1.0, and 1.2 as obtained from their XPS measurements. Figure 3d shows the dependence of elemental concentration ratio of Zn to that of Te on the VI/II flux ratio (C_{Zn}/C_{Te} in Table 2).

Dislocations in the films were studied using the surface dislocation decoration methods as described in the experimental procedures. The dislocation densities of ZnTe layers were obtained from the SEM images of Nakagawa and Everson etched samples. Figure 5 shows the post-etching SEM images of ZnTe layers grown on thermally deoxidized GaAs substrates.

The SEM images of Everson etched samples showed triangle-like shaped pits on the sample surfaces. Nakagawa et al. [37] showed that their etchants were effective at B-face of CdTe, but Fewster [38] claimed that these etchants were actually effective at the A-face of CdTe which was also confirmed with XRD studies [39]. Some studies, used Nakagawa solutions with different ratio of $HF:H_2O_2:H_2O$ to calculate the etch pit density (EPD) on the ZnTe films [40].

EPD values calculated from the SEM images of the samples are 32×10^7 cm^{-2} for sample ZT3 (Fig. 3a) and 1.7×10^7 cm^{-2} for sample ZT8 (Fig. 3c), respectively. EPD values obtained for all samples are listed in Table 2. As seen from Table 2, the sample ZT3 film grown with 1.7 IV/II flux ratio has the highest EPD, RMS roughness (R-AFM) and FWHM values indicating the worst film quality among all our films. However, for the sample ZT3, only the Everson solution was successful to create pits on the surface (Fig. 4a), but Nakagawa solution did not create dislocation pits on the surface (Fig. 4b). In contrast, Nakagawa solution was very effective for all other samples which showed smaller EPD values. Additionally, average root-mean-square (RMS) surface roughnesses obtained by AFM analyses are also listed in Table 2 as R-AFM along with film thicknesses (*t*) and VI/II flux ratios. It is obvious from the table that the EPD values and RMS roughnesses exhibit a clear correlation. In other words, both the RMS roughness and the EPD values are minimum for the samples ZT7 and ZT8, indicating that these samples are of better crystal quality than others. Thus, as the crystal quality increases the surface roughness and the dislocation densities of the films decrease.

As also seen from Table 2, increased VI/II flux ratio from 1.7 to 4.5 increases the crystal quality while going beyond 5, the quality decreases drastically as seen for the sample ZT9 with high RMS and EPD values. Also given in the table is the XPS Zn/Te ratios which is mostly about 1.2 but near 1 for better quality samples (ZT7 and ZT8). We can say that when Te flux is too high, deviations from the perfect growth conditions leads to a reduction in the Te concentration on the film surface. Therefore, the optimum VI/II growth flux ratio is about 4–4.5 at ~290 °C growth temperature.

The color intensity distribution of Nomarski microscope (NM) images were used to estimate the surface roughness of the grown ZnTe films (Fig. 5a). One way to generate a color is mixing red, green and blue (RGB) colors. The intensity variation of these three components defines the superimposed color. The absence of all three components causes black color to appear, conversely, existence of maximum intensity of all components appears as white. Intensity ranges of each color are encoded as integer numbers ranging from (0, 0, 0) to (255, 255, 255) in computers. Image information from each pixel is stored in the memory as eight-bit per color component. In an NM image, the darker pixels show the deep regions of a film surface, giving lower intensities (smaller integers) for these color components, and the bright pixels imaging the top regions of the surface, produce higher intensities (larger numbers) for these colors. The surface roughness can be calculated by taking advantage of this color intensity balance with the deep and top regions of the surface. In our analyses, from the NM images, red, green, and blue color intensity distributions were split from each other and histograms for each color distribution were obtained by means of ImageJ program. A red color intensity histogram of a NM image given in Fig. 5a, is shown in Fig. 5c. The inset was obtained by the image analysis program and it was replotted in Fig. 5c. Each color histogram curve was fitted by Voigt Model (Fig. 5c) and the FWHM

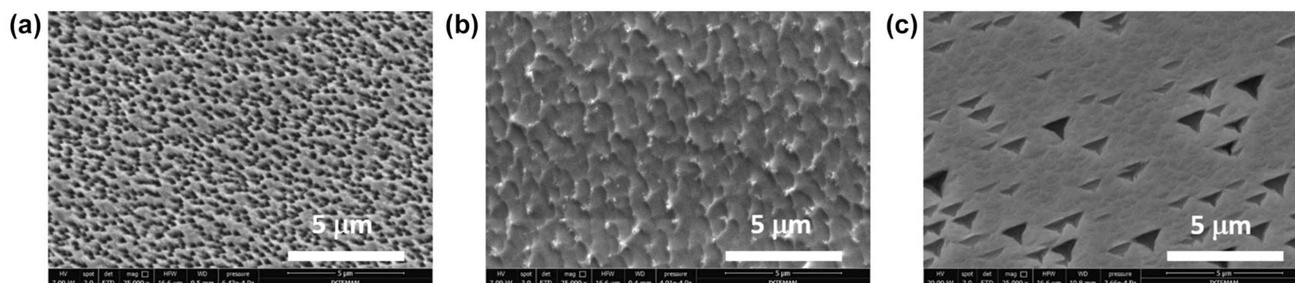

Fig. 4 SEM defect decoration images of the sample ZT3 after etching with **a** an Everson solution, **b** a Nakagawa solution, and **c**, that of the sample ZT8 etched with a Nakagawa solution

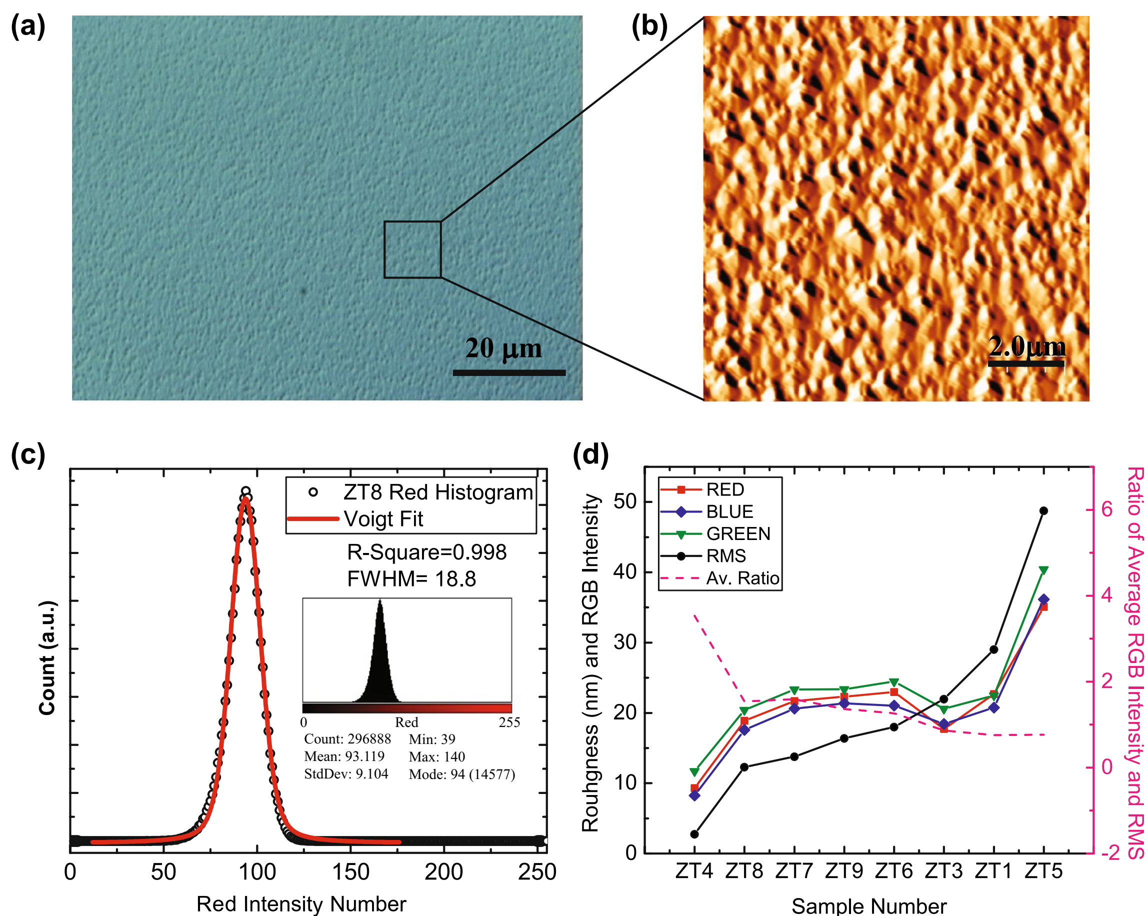

Fig. 5 Nomarski microscope image (**a**), and the AFM surface topography image of ZT8 film (**b**). The red color intensity histogram of Nomarski image in **a** is in the inset **c**. It is replotted to fit and calculate FWHM (**c**). The surface roughness RMS values obtained from the AFM topography micrographs (black), and red (red), green (green), blue (blue) color intensity histogram FWHM values (**d**). The ratio of average color histogram values to the RMS values is given as the dashed curve in **d**

values of these curves were compared with the AFM RMS roughness values of the films. The comparison is seen in Fig. 5d. All the surface roughness RMS values were calculated as the averages of at least three different topography scans as shown in Fig. 5b.

As seen in Fig. 5d, the red, green, and blue color intensity histogram FWHM values are very closely related to each other. The average FWHM value of the RGB components for each ZnTe film was divided by RMS roughness value and the ratios for all films were plotted in the figure (pink curve with the values given on the right Y axis). This ratio is close to 1 for the films with RMS roughness greater than 20 nm. Moreover, it is seen that RMS roughness value (in nanometers) remains smaller than FWHM value (in numbers) up to 20 nm beyond which it becomes greater than FWHM value. The RMS values and FWHM of the color histogram values are very compatible. Thus, we can claim that RGB color histograms of a NM image can be used to determine the surface RMS roughness value of a film qualitatively.

4 Conclusions

In this study, we investigated the effect of growth conditions on the properties of highly crystalline ZnTe films grown on GaAs (211)B substrates by MBE. The ZnTe films grown under the optimum conditions displayed an X-ray double crystal rocking curve (DCRC) FWHM value of 233 arcsecs with a 1.7×10^{7} cm^{-2} etch pit density (EPD) for a 1.66 µm thick film. It is found from XPS analyses that the ZnTe film surfaces were terminated with Te rather than Zn. Surface contamination with oxygen was lower for the films that have high crystal quality and lower surface RMS roughness and EPD values. The ZnTe films on GaAs (211)B substrates have tilt angles between 1.4° and 1.9° which is less than those for MBE grown CdTe epilayers reported in the literature. There is an inverse relation between the rocking curve FWHM and VI/II flux ratio up to 4.5 flux ratio. The best films were obtained for the VI/II flux ratios of 4.0 and 4.5. These films have relatively good crystal quality with Zn/Te

concentration ratios of about 0.9, 1.0 and 1.2. Additionally, as the crystal quality increased, the surface roughness and the dislocation densities of the films decreased. The RMS values and FWHMs of the RGB color histograms were very compatible in the range of 10–25 nm. Hence, we assert that a RGB color histogram analysis of a NM image provides a practical way to determine the RMS roughness value of a ZnTe film. This method can also be applied to films grown with other techniques with varying parameters. In conclusion, MBE-grown ZnTe films on GaAs (211)B substrates grown under optimum conditions have a great potential as a buffer layer for MCT detectors and for many other optoelectronic device applications due to their low dislocation densities and high crystal qualities.

Acknowledgements We would like to thank Orhan Öztürk, Elif Bilgilisoy, and Mustafa Polat for their help in XRD measurements. Our special thanks go to Gülnur Aygün and Lütfi Özyüzer for their support for XPS measurements. Additionally, we thank IYTE Material Research Center staff, especially Emine Bakali, for obtaining SEM images. A very heartfelt thanks and acknowledgements go to Yusuf Selamet for his support in all aspects of this work. Finally, we are grateful to SSM (Undersecretariat for Defence Industries of Turkey) and ASELSAN for their financial support.

Compliance with ethical standards

Conflict of interest On behalf of all authors, the corresponding author states that there is no conflict of interest.

References

1. L. Ouyang, J. Fan, S. Wang, X. Lu, Y.H. Zhang, X. Liu, J.K. Furdyna, D.J. Smith, J. Cryst. Growth **330**, 30–34 (2011)
2. T. Tanaka, Y. Kume, M. Nishio, Q. Guo, H. Ogawa, A. Yoshida, Jpn. J. Appl. Phys. **42**, L362–L364 (2003)
3. M. Nishio, K. Hayashida, Q. Guo, H. Ogawa, Appl. Surf. Sci. **169–170**, 227–230 (2001)
4. J.A. Garcia, A. Remón, V. Muñoz, R. Triboulet, J. Cryst. Growth **191**, 685–691 (1998)
5. T. Löffler, T. Hahn, M. Thomson, F. Jacob, H.G. Roskos, Opt. Express **13**, 5353 (2005)
6. D. Lee, J.E. Zucker, M.D. Divino, R.F. Austin, R.D. Feldman, K.L. Jones, A.M. Johnson, Appl. Phys. Lett. **59**, 1867–1869 (1991)
7. S. Valette, G. Labrunie, J. Lizet, J. Appl. Phys. **46**, 2731–2732 (1975)
8. S. Wang, D. Ding, X. Liu, X.-B. Zhang, D.J. Smith, J.K. Furdyna, Y.-H. Zhang, J. Cryst. Growth **311**, 2116–2119 (2009)
9. W. Wang, A. Lin, J.D. Phillips, J. Electron. Mater. **37**, 1044–1048 (2008)
10. W. Wang, J.D. Phillips, S.J. Kim, X. Pan, J. Electron. Mater. **40**, 1674–1678 (2011)
11. T. Tanaka, S. Kusaba, T. Mochinaga, K. Saito, Q. Guo, M. Nishio, K.M. Yu, W. Walukiewicz, Appl. Phys. Lett. **100**, 011905 (2012)
12. R.N. Jacobs, L.A. Almeida, J. Markunas, J. Pellegrino, M. Groenert, M. Jaime-Vasquez, N. Mahadik, C. Andrews, S.B. Qadri, T. Lee, M. Kim, J. Electron. Mater. **37**, 1480–1487 (2008)
13. W. Lei, R.J. Gu, J. Antoszewski, J. Dell, L. Faraone, J. Electron. Mater. **43**, 2788–2794 (2014)
14. L. He, L. Chen, Y. Wu, X.L. Fu, Y.Z. Wang, J. Wu, M.F. Yu, J.R. Yang, R.J. Ding, X.N. Hu, Y.J. Li, Q.Y. Zhang, J. Cryst. Growth **301–302**, 268–272 (2007)
15. J.P. Zanatta, G. Badano, P. Ballet, C. Largeron, J. Baylet, O. Gravrand, J. Rothman, P. Castelein, J.P. Chamonal, A. Million, G. Destefanis, S. Mibord, E. Brochier, P. Costa, J. Electron. Mater. **35**, 1231–1236 (2006)
16. J.M. Arias, J. Vac. Sci. Technol. B Microelectron. Nanom. Struct. **9**, 1646 (1991)
17. S. Rujirawat, L.A. Almeida, Y.P. Chen, S. Sivananthan, D.J. Smith, Appl. Phys. Lett. **71**, 1810–1812 (1997)
18. R.N. Jacobs, M. Jaime Vasquez, C.M. Lennon, C. Nozaki, L.A. Almeida, J. Pellegrino, J. Arias, C. Taylor, B. Wissman, J. Electron. Mater. **44**, 3076–3081 (2015)
19. L. He, X. Fu, Q. Wei, W. Wang, L. Chen, Y. Wu, X. Hu, J. Yang, Q. Zhang, R. Ding, X. Chen, W. Lu, J. Electron. Mater. **37**, 1189–1199 (2008)
20. J. Chai, O.C. Noriega, A. Dedigama, J.J. Kim, A.A. Savage, K. Doyle, C. Smith, N. Chau, J. Pena, J.H. Dinan, D.J. Smith, T.H. Myers, J. Electron. Mater. **42**, 3090–3096 (2013)
21. J. Fan, L. Ouyang, X. Liu, D. Ding, J.K. Furdyna, D.J. Smith, Y.-H. Zhang, J. Cryst. Growth **323**, 127–131 (2011)
22. M.S. Jang, S.H. Oh, K.H. Lee, J.H. Bahng, J.C. Choi, K.H. Jeong, H.L. Park, D.C. Choo, D.U. Lee, T.W. Kim, J. Phys. Chem. Solids **64**, 357–360 (2003)
23. Q. Guo, K. Takahashi, K. Saito, H. Akiyama, T. Tanaka, M. Nishio, Appl. Phys. Lett. **102**, 092107 (2013)
24. O. Arı, E. Bilgilisoy, E. Ozceri, Y. Selamet, J. Electron. Mater. **45**, 4736–4741 (2016)
25. E. Bilgilisoy, S. Özden, E. Bakali, M. Karakaya, Y. Selamet, J. Electron. Mater. **44**, 3124–3133 (2015)
26. J. Frühauf, E. Gärtner, S. Krönert, *Shape and Functional Elements of the Bulk Silicon Microtechnique* (Springer, Berlin, 2005)
27. W.J. Everson, C.K. Ard, J.L. Sepich, B.E. Dean, G.T. Neugebauer, H.F. Schaake, J. Electron. Mater. **24**, 505–510 (1995)
28. E.P. Warekois, M.C. Lavine, A.N. Mariano, H.C. Gatos, J. Appl. Phys. **33**, 690–696 (1962)
29. M.J. Fairlie, J.G. Akkerman, R.S. Timsit, J.M. Zavislan, in *Proceedings of SPIE 0749, Metrology: Figure and Finish* (1987), pp. 105–113
30. W. Mönch, *Semiconductor Surfaces and Interfaces* (Springer, Berlin, 2001)
31. L.Q. Zhou, C. Chen, H. Jia, C. Ling, D. Banerjee, J.D. Phillips, Y. Wang, J. Electron. Mater. **43**, 889–893 (2014)
32. W. Mahmood, A. Thomas, A.U. Haq, N.A. Shah, M.F. Nasir, J. Phys. D. Appl. Phys. **50**, 255503 (2017)
33. Z. Zhang, B. Wang, P. Zhou, R. Kang, B. Zhang, D. Guo, Sci. Rep. **6**, 26891 (2016)
34. X.J. Wang, Y.B. Hou, Y. Chang, C.R. Becker, R.F. Klie, S. Sivananthan, J. Electron. Mater. **38**, 1776–1780 (2009)
35. S.Y. Woo, G.A. Devenyi, S. Ghanad-Tavakoli, R.N. Kleiman, J.S. Preston, G.A. Botton, Appl. Phys. Lett. **102**, 132103 (2013)
36. O. Arı, M. Polat, M. Karakaya, Y. Selamet, Phys. Status Solidi **12**, 1211–1214 (2015)
37. K. Nakagawa, K. Maeda, S. Takeuchi, Appl. Phys. Lett. **34**, 574–575 (1979)
38. P.F. Fewster, S. Cole, A.F.W. Willoughby, M. Brown, J. Appl. Phys. **52**, 4568–4571 (1981)
39. P.F. Fewster, P.A.C. Whiffin, J. Appl. Phys. **54**, 4668–4670 (1983)
40. T. Asahi, T. Yabe, K. Sato, J. Electron. Mater. **33**, 651–653 (2004)

Publisher's Note Springer Nature remains neutral with regard to jurisdictional claims in published maps and institutional affiliations.